Ultrasound in Med. & Biol., Vol. 48, No. 1, pp. 149–156, 2022

0301-5629/$ - see front matter

https://doi.org/10.1016/j.ultrasmedbio.2021.09.009

● *Technical Note*

SPATIOTEMPORAL DISTRIBUTION OF NANODROPLET VAPORIZATION IN A PROTON BEAM USING REAL-TIME ULTRASOUND IMAGING FOR RANGE VERIFICATION

Gonzalo Collado-Lara,* Sophie V. Heymans,*,†,‡ Marta Rovituso,§ Bram Carlier,¶ Yosra Toumia,‖ Martin Verweij,*,** Gaio Paradossi,‖ Edmond Sterpin,¶ Hendrik J. Vos,*,** Jan D'hooge,‡ Nico de Jong,*,** Koen Van Den Abeele,† and Verya Daeichin**

* Biomedical Engineering, Department of Cardiology, Erasmus MC University Medical Center, Rotterdam, The Netherlands; † Department of Physics, KU Leuven Campus Kulak, Kortrijk, Belgium; ‡ Department of Cardiovascular Sciences, KU Leuven, Leuven, Belgium; § Holland Proton Therapy Center, Delft, The Netherlands; ¶ Department of Oncology, KU Leuven, Leuven, Belgium; ‖ Department of Chemical Sciences and Technology, University of Rome Tor Vergata, Rome, Italy; and ** Department of Medical Imaging, TU Delft, Delft, The Netherlands

(*Received* 23 *June* 2021; *revised* 6 *September* 2021; *in final form* 7 *September* 2021)

Abstract—The potential of proton therapy to improve the conformity of the delivered dose to the tumor volume is currently limited by range uncertainties. Injectable superheated nanodroplets have recently been proposed for ultrasound-based *in vivo* range verification, as these vaporize into echogenic microbubbles on proton irradiation. In previous studies, offline ultrasound images of phantoms with dispersed nanodroplets were acquired after irradiation, relating the induced vaporization profiles to the proton range. However, the aforementioned method did not enable the counting of individual vaporization events, and offline imaging cannot provide real-time feedback. In this study, we overcame these limitations using high-frame-rate ultrasound imaging with a linear array *during* proton irradiation of phantoms with dispersed perfluorobutane nanodroplets at 37°C and 50°C. Differential image analysis of subsequent frames allowed us to count individual vaporization events and to localize them with a resolution beyond the ultrasound diffraction limit, enabling spatial and temporal quantification of the interaction between ionizing radiation and nanodroplets. Vaporization maps were found to accurately correlate with the stopping distribution of protons (at 50°C) or secondary particles (at both temperatures). Furthermore, a linear relationship between the vaporization count and the number of incoming protons was observed. These results indicate the potential of real-time high-frame-rate contrast-enhanced ultrasound imaging for proton range verification and dosimetry. (E-mail: g.colladolara@erasmusmc.nl)

Key Words: **Proton therapy, Ultrasound, Nanodroplets, Range verification, Dosimetry.**

INTRODUCTION

Proton therapy is emerging as an advanced radiation therapy modality for tumors in critical locations (Grau et al. 2020). Because protons deposit most of their dose in a narrow (few millimeters wide) peak at the end of their range, called the Bragg peak, followed by a sharp distal dose fall-off, the spatial dose distribution can be better conformed to the tumor volume than in conventional radiotherapy, thereby improving healthy tissue sparing (Parodi and Polf 2018). In practice, however, the physical benefits of protons cannot be fully exploited because deviations from the planned dose distribution may arise from different sources of range uncertainty, including treatment planning, setup errors and patient and organ motion (Paganetti 2012; Knopf and Lomax 2013). Therefore, substantial safety margins are included in the treatment plan (Paganetti 2012; Polf and Parodi 2015), reducing the potential improvement compared with conventional radiotherapy. The benefits of proton therapy could be maximized if deviations during the treatment were detected and

Address correspondence to: Gonzalo Collado-Lara, Erasmus MC, Ee23.02, PO Box 2040, 3000 CA Rotterdam, The Netherlands. E-mail: g.colladolara@erasmusmc.nl

Gonzalo Collado-Lara and Sophie V. Heymans contributed equally to this work.

corrected through real-time spatial verification, especially in moving targets (Kubiak 2016; Meijers et al. 2020; Raldow et al. 2020). Although several *in vivo* range verification techniques are being investigated (Parodi et al. 2007; Zhu et al. 2011; Lehrack et al. 2017; Xie et al. 2017; Hickling et al. 2018; Patch et al. 2021), none of them has been widely adopted in clinical practice.

The detection of charged particles, among which are protons, can be achieved in superheated liquids (D'Errico 2001; Felizardo et al. 2013; Miller et al. 2018), which can remain in a metastable liquid phase above their boiling point owing to the removal of heterogeneous nucleation sites (Apfel 1979). The only mechanism remaining for vaporization is homogeneous nucleation, occurring when a gas embryo grows larger than a critical size (Mountford and Borden 2016). Consequently, a charged particle can induce vaporization of the superheated liquid if it deposits a sufficient amount of energy to nucleate such a critical embryo within a length comparable to the embryo size (D'Errico 2001). Accordingly, the condition for vaporization of superheated liquids depends on the density of energy deposited by the charged particle per unit length, namely, its linear energy transfer (LET). Furthermore, the energy necessary to nucleate a critical embryo decreases with the temperature excess above the liquid boiling point, that is, the degree of superheat (D'Errico 2001).

Superheated nanodroplets have been introduced as a novel injectable ultrasound contrast agent capable of turning into echogenic microbubbles on controlled energy deposition, for example, acoustic or thermal (Sheeran et al. 2012; Shimizu et al. 2012; Dove et al. 2014; Lin et al. 2017; Toumia et al. 2019). It was only recently reported that the phase-change mechanism holds for superheated encapsulated nanodroplets irradiated by protons (Carlier et al. 2020; Heymans et al. 2021). The combination of the longstanding knowledge of radiation-induced nucleation with the recent developments in producing stable, injectable nanodroplets opens the door to ultrasound-based detection and monitoring of ionizing radiation *in vivo*.

Previous studies of nanodroplet vaporization using a passively scattered proton beam have demonstrated a sub-millimeter reproducibility of the shift between the proton range and vaporization profiles derived from the ultrasound gray value or attenuation coefficient (Carlier et al. 2020; Heymans et al. 2021). However, offline ultrasound imaging does not enable real-time verification and, potentially, compensation of deviations during treatment delivery. Moreover, those studies revealed the presence of acoustic shadowing and image saturation, which led to a complex relation between ultrasound contrast and proton fluence (Soetanto and Chan 2000), limiting the performance for dosimetry and range verification. Indeed, obtaining a sufficient response for accurate range verification and dosimetry *in vivo* will require high bubble concentrations, which precludes individual bubble counting on offline ultrasound images. Moreover, real-time verification during proton therapy would allow the beam to be stopped during the treatment in case of deviation. Online imaging would be performed with the patient in the treatment position, and could be more robust to potential errors induced by nanodroplets and microbubble biological washout, compared with offline, post-irradiation imaging. Therefore, in this study, we transition to real-time high-frame-rate ultrasound imaging during irradiation in a proton beam to detect individual vaporization events and localize them with an accuracy beyond the ultrasound diffraction limit. This allowed temporal and spatial quantification of the interaction between charged particles and superheated nanodroplets.

METHODS

Nanodroplet and phantom synthesis

Nanodroplets with a perfluorobutane core (boiling point −2°C) and a crosslinked polymeric shell made of polyvinyl alcohol (PVA) were prepared according to the protocol described by Heymans et al. (2021). Briefly, gaseous perfluorobutane was injected in an empty vial and liquefied by immersion in liquid nitrogen. After addition of an aqueous telechelic PVA solution (2% w/v PVA, 0.2% w/v sodium metaperiodate), the vial was sonicated in an ice-cold water bath for 15 min. The resulting nanodroplets were then washed by a two-step centrifugation. Dynamic light scattering measurements yielded intensity-weighted size distributions with a median nanodroplet size of 799 nm and a polydispersity index of 0.3 (Heymans et al. 2021). The droplets were dispersed in an aqueous polymer gel, which entrapped their position, to achieve a homogeneous distribution within the phantom. The phantom matrix was made of a carbomer solution (0.1% w/v) and prepared according to Putz and Burghelea (2009): after dilution of Carbopol 2050 powder (Lubrizol, Wickliffe, OH, USA) in Milli-Q water, the solution pH was adjusted to 7 by adding NaOH while monitoring with a pH meter (Consort C830, Turnhout, Belgium). This non-Newtonian fluid was able to entrap the nanodroplets and resulting microbubbles, keeping the dispersion of contrast agents homogeneous throughout the experiment, but did not impede the microbubble oscillations (Brunet et al. 2012). Before nanodroplet dispersion, the carbomer solution and phantom containers (54 × 26 × 31 mm) were first heated to the desired temperature (37°C or 50°C). Then, the carbomer solution was poured into phantom containers

(54 × 26 × 31 mm), and a given volume of nanodroplets was dispersed homogeneously in the gel by manual stirring. The phantoms were subsequently immersed in a water tank preheated to 37˚C or 50˚C for irradiation. The perfluorobutane concentration in the phantom was assessed with nuclear magnetic resonance (NMR) spectroscopy (400-MHz Avance II, Bruker Biospin GmbH, Rheinstetten, Germany) on the day following the proton experiments and was 19 μM. For this concentration, the impact of both liquid-filled nanodroplets and gas-filled microbubbles on proton therapy treatment delivery (*i.e.,* the proton range) is expected to be negligible.

Phantom irradiation

The phantoms were irradiated in the research beam line of the Holland Proton Therapy Center in Delft (HPTC). The water tank was aligned to have its outer wall positioned at the beam isocenter and the phantom traversed by the proton beam through its center (Fig. 1a). Reproducibility of phantom positioning with respect to the proton range was ensured with a locking pin. The distance between the water tank's outer wall and the phantom entrance was 13.3 cm. The R&D proton room of HPTC has a horizontal, fixed beam line which provides a therapeutic beam from 70 to 250 MeV with beam intensities from 1 to 800nA at beam extraction. A beam energy of 154 MeV was chosen to ensure that the proton range would approximately correspond to the phantom midlength, as illustrated in Figure 1a. As the accelerator produced a single pencil beam, the lateral beam profile was a 2-D Gaussian. For each irradiation, the total number of protons was counted with an ionization chamber (beam monitor, DE.TEC.TOR, Torino, Italy) inserted in the beam path (Fig. 1a). The beam currents, total number of protons, irradiation durations and phantom doses are given in Table 1. The radiation dose used at 50˚C was relatively close to the typical dose delivered in a proton therapy session (~2 Gy), while a higher dose was used at 37˚C to account for the fact that at this temperature, nanodroplets are sensitive only to high-LET secondary particles, which are relatively rare (Heymans et al. 2021).

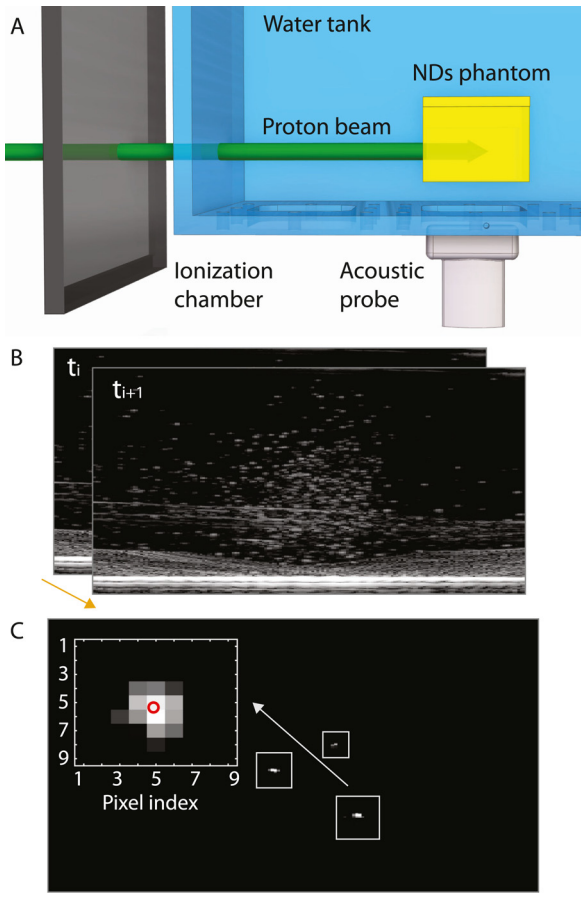

Fig. 1. (a) Schematic representation of the setup. The proton beam was used to irradiate nanodroplets (NDs) dispersed in a phantom (*yellow*), which was imaged in real time with an ultrasound array. Simultaneously, an ionization chamber counted the incoming protons. (b) Subsequent frames were subtracted to isolate vaporization events. (c) Example of differential

Characterization of the proton beam

The spatial dimensions of the proton beam were independently characterized after the experiment. The depth−dose distribution was measured using a multilayer ionization chamber (QubeNext, 2.43 mm spacing, DE.TEC.TOR) and fit to an analytical expression of the Bragg curve (Bortfeld 1997) to obtain the proton range R_{80} (*i.e.,* distal position at which the dose has dropped to 80% of its peak value [Paganetti 2012, 2019]). The impact of the in-beam ionization chamber, water tank entrance wall (9.5 mm, polymethyl methacrylate) and phantom container entrance wall (2 mm, PVC) on the range was estimated by calculating their water equivalent thickness (Zhang and Newhauser 2009). The phantom was considered water equivalent, as it was made of 99.9% water. As nanodroplets are vaporized by individual charged particles at the end of their range (*i.e.,* where the LET is maximal), the distributions of their ranges (also called "stopping distributions") were computed to be compared with nanodroplet vaporization maps. The stopping distribution of primary protons in the beam direction was modeled as a Gaussian centered on the R_{80} position, defined as "the depth at which half the surviving primaries ... have stopped" (Paganetti 2019). The standard deviation, characterizing the range dispersion, was obtained from the analytical Bragg curve fit. The entrance lateral spot profile was measured at the isocenter with a scintillating screen detector (LynxPT, IBA

Table 1. Irradiation settings

Phantom	Temperature (˚C)	Cyclotron current (nA)	No. of incoming protons	Irradiation time (s)	Peak dose (Gy)	Averaged dose across Gaussian FWHM at Bragg peak (Gy)
1	37	80	7.96×10^9	4.93	14.19	9.25
2	50	25	2.61×10^9	5.20	4.65	3.03

FWHM = full width half-maximum.

Dosimetry, Schwarzenbruck, Germany). Lateral spot spreading in water was modeled using a Gaussian approximation and applying the Highland formula (Gottschalk et al. 1993; Paganetti 2019). The combination of the beam model and online proton count enabled computation of the 3-D proton stopping distribution and absorbed dose for each phantom. Aside from protons, nanodroplets can also be vaporized by heavy secondary particles, which are produced by nuclear reactions between primary protons and atomic nuclei from the medium. As those secondary particles have a very limited range (few microns), contrarily to protons, their stopping distribution was assimilated to their production distribution. The spatial distributions of secondary reaction products generated from the nuclear reaction $p + {}^{16}O$ were also derived from the production cross-section of relevant particles (International Commission on Radiation Units & Measurements [ICRU] 2000).

Online ultrasound imaging and image processing

Real-time ultrasound imaging during proton irradiation was achieved by fixing a linear ultrasound array (ATL L12-5, 38-mm aperture) outside the water tank (acoustic coupling was ensured through ultrasound gel and a 20-μm polyester window) (Fig. 1a). The side of the phantom facing the ultrasound probe was also covered with an identical acoustically transparent window. The array was connected to a research platform (Verasonics Vantage 256, Kirkland, WA, USA) to image phantoms at 1000 frames/s during irradiation, by use of a plane wave (0˚, no angle compounding) imaging sequence. The ultrasound center frequency was 9 MHz, and the peak negative pressure of the plane waves was 370 kPa (characterized with a 0.075-mm needle hydrophone, Precision Acoustics, Dorchester, England), well below the threshold for acoustic droplet vaporization (Sheeran et al. 2010). The ultrasound radiofrequency (RF) data were beamformed offline using the Verasonics beamformer. Differential imaging was performed by subtracting subsequent frames (Fig. 1b), allowing identification of newly formed echogenic microbubbles (radiation-induced vaporized nanodroplets), which appeared as bright spots in the subtracted frames (Fig. 1c). As the vaporization events per frame were sparse, they could be individually detected as in ultrasound localization microscopy (Hingot et al. 2016; Zhang et al. 2018), with a resolution overcoming the ultrasound diffraction limit (<50 μm) (Viessmann et al. 2013; Errico et al. 2015). The events were detected in the differential images by intensity thresholding and localized by the weighted average centroid of their point spread function. To determine the distance between the ultrasound probe and the entrance of the proton beam, a fiducial object of known absolute position was imaged between irradiations. This step provided us with an absolute reference in the direction parallel to the beam to compare range estimates from the obtained vaporization maps with ionization chamber measurements. In the direction orthogonal to the beam, the distance between the beam axis and the probe was not measured. Therefore, the vaporization counts and the beam profile in the orthogonal direction were aligned during post-processing.

RESULTS AND DISCUSSION

Influence of the temperature on the vaporization response

Videos of the ultrasound B-mode frames, differential images and accumulated vaporization events are available online as Supplementary Data. The 2-D maps of the vaporized nanodroplets detected during proton irradiation at 37˚C and 50˚C are provided in Figure 2. A considerable difference in vaporization density and location can be observed for the two temperatures, with the presence of sparse vaporization events mostly in front of the Bragg peak (dose peak) at 37˚C (Fig. 2a) and a high vaporization density close to the proton range at 50˚C (Fig. 2b). We attribute this difference to the variation of the LET threshold for vaporization with temperature, leading to the detection of different charged particles. It was previously reported for the droplets used in these experiments that at moderate degrees of superheat, vaporization is induced by high-LET secondary particles only (Carlier et al. 2020; Heymans et al. 2021), which can be produced by nuclear reactions up until the proton energy drops below the Coulomb barrier (the energy barrier that protons should overcome to trigger a nuclear reaction with an atom from the medium). Only at high degrees of superheat is the vaporization threshold sufficiently low (<70 keV/μm) for protons to directly

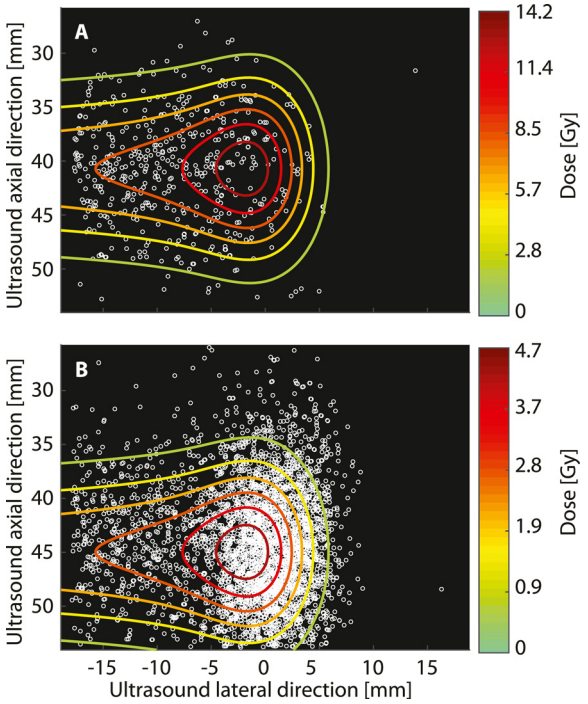

Fig. 2. Vaporization maps at 37˚C (a) and 50˚C (b) overlaid with the beam dose distribution (the field of view limits match the phantom dimensions). The same nanodroplet concentration was employed in both phantoms, while the maximum dose was higher at 37˚C.

vaporize nanodroplets at their individual Bragg peak (Heymans et al. 2021). This explains the enhancement observed in Figure 2b at the proton range (where the majority of the primary protons stop), just beyond the dose maximum. The difference in number of vaporization events stems from the fact that non-elastic nuclear reactions are relatively rare events (1% per centimeter [Durante and Paganetti 2016]), yielding a number of secondary particles much lower than primary protons. At 50˚C, the bubble density within the peak zone after irradiation was too high to allow the localization of single bubbles on post-irradiation images, highlighting the need for high-frame-rate differential imaging.

Spatial quantification of the vaporization events

Because vaporization events were not expected to be directly proportional to the absorbed dose, but rather to be related to the number of stopping primary protons and secondaries, the spatial distribution of bubble count was compared with these beam features (Fig. 3). Two-dimensional maps are represented in Figures 3a1 and 3b1 for 37˚C and 50˚C, respectively. Vaporization count profiles were obtained by binning the location of all vaporization events in the direction parallel (Fig. 3a2, 3b2) and orthogonal (Fig. 3a3, 3b3) to the proton beam. Here, the *red color* was used to display the spatial distribution of the stopping positions of individual protons inside the phantom, and the *blue color* represents the spatial density of relevant secondary particles.

At 37˚C, the microbubble count profiles are compared with the spatial distribution of heavy secondaries ($Z > 1$), as those are expected to have a sufficient LET to vaporize nanodroplets (Heymans et al. 2021).

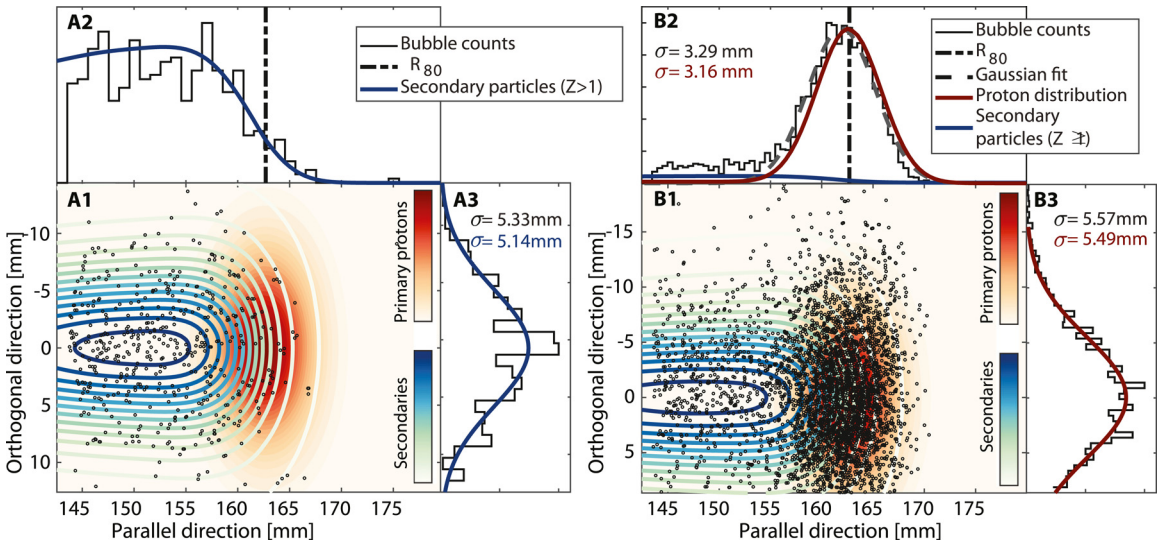

Fig. 3. Nanodroplet vaporization distribution at 37˚C (a1) and 50˚C (b1) superimposed on the distribution of the stopping positions of primary protons (*red color scale*) and heavy secondaries ($Z > 1$ [a1] or $Z \geq 1$ [b1], *blue color scale*). The vaporization counts were projected in the direction parallel (a2, b2) and orthogonal (a3, b3) to the proton beam, and compared with the corresponding projections of the stopping distribution of secondary particles (a2, a3) and primary protons (b2, b3). The proton range is represented by a *dashed vertical line* (a2 and b2). The standard deviations (σ) are displayed for both the bubble count profiles (Gaussian fit) and the charged particle profiles.

Qualitatively, bubble count profiles closely resemble the distribution of secondaries (Fig. 3a2, 3a3). To compare the lateral spot spreading with the bubble count profile (Fig. 3a3), a Gaussian fit was applied to the latter, yielding a standard deviation (σ = 5.33 mm) close to the dispersion of secondaries (σ = 5.14 mm). At 50˚C, the projection of the microbubble counts on the axis parallel to the proton beam (Fig. 3b2) clearly illustrates that vaporization is induced both by primary protons at the end of their range, responsible for the observed Gaussian peak, and by secondaries ($Z \geq 1$, including secondary protons), responsible for the plateau proximal to the proton range. This is further supported by the sub-millimeter distance (0.8 mm) between the peak in bubble count (161.9 mm) and the peak in stopping protons (162.7 mm, R_{80} position), which we attribute to experimental uncertainties. Importantly, the position of the vaporization count peak, including an uncertainty window of $\pm 3\sigma$, was within $\pm$0.5 mm of its final value from 575 events on, indicating that for the tested nanodroplet concentration, a dose of 0.7 Gy (dose maximum reported at the spot center) would have been sufficient to obtain a range estimate with $\pm$0.5-mm precision. Moreover, the standard deviation for the bubble count (Gaussian fit) was within 0.2 mm of that of the range (Fig. 3b2) and within 0.1 mm of the beam lateral standard deviation (Fig. 3b3).

Overall, the profiles in Figure 3 illustrate the ability of the obtained vaporization maps to accurately represent different spatial features of the proton beam, depending on the temperature. This has implications not only for range verification, as bubble count profiles can be directly (50˚C) or indirectly (37˚C) related to the proton range, but also for dosimetry, as both the number of activated droplets and their spatial distribution can be accurately quantified. The ratio between the microbubble peak and its plateau at 50˚C (9.31) is smaller than the ratio between primary protons and secondaries (25.5), possibly because the vaporization efficiency depends on the charged particle type (D'Errico 1999). Also, the standard deviation of the microbubble Gaussian distribution only slightly exceeds the proton stopping dispersion (by 4%), while it was largely overestimated (by >100%) on previous post-irradiation offline recordings (Heymans et al. 2021). To summarize, online high-frame-rate imaging was found to be a reliable tool to characterize the interaction of nanodroplets with ionizing radiation.

Temporal quantification of the vaporization events

Next to spatial quantification, online ultrasound imaging allowed examination of the temporal vaporization rate and assessment of the relationship between the vaporization counts and the proton fluence. Figure 4a compares the cumulative number of vaporization events

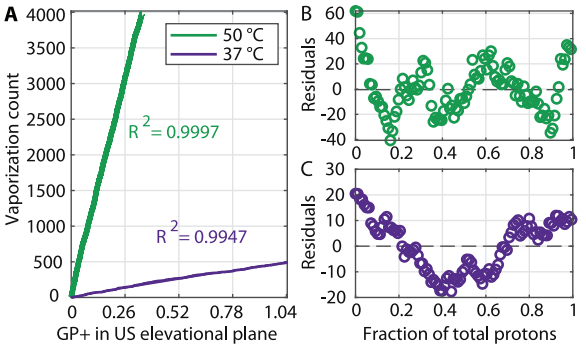

Fig. 4. (a) Vaporization count as a function of number of stopping protons in the ultrasound (US) field of view (GP+ symbol refers to 10^9 protons). The R^2 values and residual counts of a linear fit are shown both at 50˚C (b) and 37˚C (c).

recorded during irradiation with the number of stopping protons in the field of view of the ultrasound probe (the elevational plane thickness was approximated to a quarter of the elevational aperture [Cobbold 2006]). We assumed a constant proton flux during irradiation, neglecting any small deviation in beam current. The results indicate a linear relationship between the number of vaporization events and the number of protons, with coefficients of determination of 0.9947 at 37˚C and 0.9997 at 50˚C. In comparing both temperatures, a 25-fold increase in the number of generated microbubbles was observed, from 460 bubbles per 10^9 stopping protons at 37˚C to 11.6 $\times$ 10^3 bubbles per 10^9 stopping protons at 50˚C. The residuals are illustrated in Figure 4b, 4c and have root mean square errors of 10 events at 37˚C and 19.5 events at 50˚C. The maximum deviation occurred at the start of the irradiation in both cases, which could be caused by the beam "ramp-up." The linearity of these curves indicates a straightforward relationship between proton and vaporization count, which could potentially be exploited for dosimetry. However, the influence of the nanodroplet concentration and proton dose on linearity should be addressed in future studies, as both acoustic shadowing and a gradual decrease in nanodroplet concentration (caused by radiation-induced vaporization) in regions with high densities of vaporization events might reduce the count rates.

Future directions and clinical translation

Two scenarios are presented here: sensitivity only to high-LET secondaries (37˚C) and sensitivity to primaries and secondaries (50˚C). The current nanodroplets were sensitive to secondary reaction products at physiological temperature, which could be used to indirectly measure the range *in vivo* with an approach similar to positron emission tomography (PET) and prompt gamma imaging. However, the number of vaporization events was multiplied by a factor of 25 at 50˚C, once they became sensitive

to primary protons. A larger number of events will utterly result in a refined resolution for both dosimetry and range verification. Moreover, vaporization by primary protons leads to a direct relationship between the peak in vaporization count and the proton range. Therefore, even though the indirect response observed at 37°C for our nanodroplet formulation might enable proton range verification, increasing the degree of superheat of the nanodroplets to transpose the direct response to physiological temperature would be desirable (Heymans et al. 2021). This could be achieved by modifying the nanodroplet liquid core using lower-boiling-point perfluorocarbons (Mountford and Borden 2016) or mixed compounds (Shakya et al. 2020).

This *in vitro* study was performed under ideal conditions as a proof of concept; thus, future research should cover different aspects with respect to clinical translation. The effects of both tissue and nanodroplet distribution inhomogeneities on the accuracy of the localization method should be assessed and compared with the homogeneous dispersions used here. In particular, the use of acoustic droplet vaporization as a calibration tool could be considered, to infer potential nanodroplet distribution inhomogeneities. Furthermore, analytical models need to be developed to estimate the nanodroplet response for complex treatment plans, and the integration of the ultrasound system in the proton therapy room should be examined. Ultimately, we envision that this online range verification method could benefit several sites of sonic accessibility such as the prostate, breast and liver. In the longer term, the dosimetric use of nanodroplets could be complemented with their ability to mechanically (through cavitation) or chemically (through drug or oxygen delivery) enhance the tumor response to radiation therapy (Czarnota et al. 2012; Lacerda et al. 2021).

Finally, even though the detection and localization of vaporization events were performed offline, the necessary operations were not too computationally intensive. Thus, future research could focus on the optimization and implementation of the algorithm in real time (Ramalli et al. 2018, 2020) to provide direct feedback over the course of irradiation.

CONCLUSIONS

We have developed and implemented a method for detecting and superlocalizing superheated nanodroplet vaporization events in a proton pencil beam using high-frame-rate contrast-enhanced ultrasound imaging. This allowed quantification of the spatial and temporal distributions of droplet activation events, which have been related to the proton range as well as to spatial features of primary protons and secondary particles. The method described method allows derivation of microbubble count profiles directly representing the interaction between nanodroplets and charged particles, even for large vaporization concentrations for which offline ultrasound assessment would provide only indirect information. Ultimately, online imaging could provide real-time feedback during proton therapy, potentially enabling compensation for deviations in treatment delivery.

CONFLICT OF INTEREST DISCLOSURE

The authors declare no conflict of interest.

Acknowledgments—This study was funded by the European Union's Horizon 2020 research and innovation program under Grant Agreement No. 766456 ("AMPHORA") and by the Dutch Research Council under Grant NWA 1160.18.095.

The authors thank A. A. Brouwer (Erasmus MC), R. Beurskens (Erasmus MC) and H. den Bok (TU Delft) for their help in designing and building the experimental apparatus.

SUPPLEMENTARY MATERIALS

Supplementary material associated with this article can be found in the online version at doi:10.1016/j.ultrasmedbio.2021.09.009.

REFERENCES

Apfel RE. The superheated drop detector. Nucl Instruments Methods 1979;162:603–608.

Bortfeld T. An analytical approximation of the Bragg curve for therapeutic proton beams. Med Phys 1997;24:2024–2033.

Brunet T, Raffy S, Mascaro B, Leng J, Wunenburger R, Mondain-Monval O, Poncelet O, Aristégui C. Sharp acoustic multipolar-resonances in highly monodisperse emulsions. Appl Phys Lett 2012;101 011913.

Carlier B, Heymans SV, Nooijens S, Toumia Y, Ingram M, Paradossi G, D'Agostino E, Himmelreich U, D'Hooge J, Van Den Abeele K, Sterpin E. Proton range verification with ultrasound imaging using injectable radiation sensitive nanodroplets: A feasibility study. Phys Med Biol 2020;65 065013.

Cobbold RSC. Foundations of biomedical ultrasound. London/New York: Oxford University press; 2006.

Czarnota GJ, Karshafian R, Burns PN, Wong S, Al Mahrouki A, Lee JW, Caissie A, Tran W, Kim C, Furukawa M, Wong E, Giles A. Tumor radiation response enhancement by acoustical stimulation of the vasculature. Proc Natl Acad Sci USA 2012;109:E2033–E2041.

D'Errico F. Fundamental properties of superheated drop (bubble) detectors. Radiat Prot Dosimetry 1999;84:55–62.

D'Errico F. Radiation dosimetry and spectrometry with superheated emulsions. Nucl Instrum Methods Phys Res Sect B Beam Interact Mater Atoms 2001;184:229–254.

Dove JD, Mountford PA, Murray TW, Borden MA. Engineering optically triggered droplets for photoacoustic imaging and therapy. Biomed Opt Express 2014;5:4417.

Durante M, Paganetti H. Nuclear physics in particle therapy: A review. Rep Prog Phys 2016;79 096702.

Errico C, Pierre J, Pezet S, Desailly Y, Lenkei Z, Couture O, Tanter M. Ultrafast ultrasound localization microscopy for deep super-resolution vascular imaging. Nature 2015;527:499–502.

Felizardo M, Morlat T, Marques JG, Ramos AR, Girard TA, Fernandes AC, Kling A, Lázaro I, Martins RC, Puibasset J. Fabrication and response of high concentration SIMPLE superheated droplet detectors with different liquids. Astropart Phys 2013;49:28–43.

Gottschalk B, Koehler AM, Schneider RJ, Sisterson JM, Wagner MS. Multiple Coulomb scattering of 160 MeV protons. Nucl Instrum

Methods Phys Res Sect B Beam Interact Mater Atoms 1993;74:467–490.
Grau C, Durante M, Georg D, Langendijk JA, Weber DC. Particle therapy in Europe. Mol Oncol 2020;14:1492–1499.
Heymans SV, Carlier B, Toumia Y, Nooijens S, Ingram M, Giammanco A, D'Agostino E, Crijns W, Bertrand A, Paradossi G, Himmelreich U, D'Hooge J, Sterpin E, Van Den Abeele K. Modulating ultrasound contrast generation from injectable nanodroplets for proton range verification by varying the degree of superheat. Med Phys 2021;48:1983–1995.
Hickling S, Xiang L, Jones KC, Parodi K, Assmann W, Avery S, Hobson M, El Naqa I. Ionizing radiation-induced acoustics for radiotherapy and diagnostic radiology applications. Med Phys 2018;45:707–721.
Hingot V, Bézagu M, Errico C, Desailly Y, Bocheux R, Tanter M, Couture O. Subwavelength far-field ultrasound drug-delivery. Appl Phys Lett 2016;109(19).
International Commission on Radiation Units & Measurements (ICRU). Nuclear data for neutron and proton radiotherapy and for radiation protection, ICRU Rep. No. 63. Bethesda, MD: Author; 2000.
Knopf AC, Lomax A. In vivo proton range verification: A review. Phys Med Biol 2013;58:131–160.
Kubiak T. Particle therapy of moving targets—The strategies for tumour motion monitoring and moving targets irradiation. Br J Radiol 2016;89 20150275.
Lacerda Q, Tantawi M, Leeper DB, Wheatley MA, Eisenbrey JR. Emerging applications of ultrasound-contrast agents in radiation therapy. Ultrasound Med Biol 2021;47:1465–1474.
Lehrack S, Assmann W, Bertrand D, Henrotin S, Herault J, Heymans V, Vander Stappen F, Thirolf PG, Vidal M, Van de Walle J, Parodi K. Submillimeter ionoacoustic range determination for protons in water at a clinical synchrocyclotron. Phys Med Biol 2017;62:L20–L30.
Lin S, Shah A, Hernández-Gil J, Stanziola A, Harriss BI, Matsunaga TO, Long N, Bamber J, Tang MX. Optically and acoustically triggerable sub-micron phase-change contrast agents for enhanced photoacoustic and ultrasound imaging. Photoacoustics 2017;6:26–36.
Meijers A, Seller OC, Free J, Bondesson D, Seller Oria C, Rabe M, Parodi K, Landry G, Langendijk JA, Both S, Kurz C, Knopf AC. Assessment of range uncertainty in lung-like tissue using a porcine lung phantom and proton radiography. Phys Med Biol 2020;65 155014.
Miller A, Machrafi R, Benton E, Kitamura H, Kodaira S. Comparison of the space bubble detector response to space-like neutron spectra and high energy protons. Acta Astronaut 2018;151:1–6.
Mountford PA, Borden MA. On the thermodynamics and kinetics of superheated fluorocarbon phase-change agents. Adv Colloid Interface Sci 2016;237:15–27.
Paganetti H. Range uncertainties in proton therapy and the role of Monte Carlo simulations. Phys Med Biol 2012;57:R99–R117.
Paganetti H. Proton therapy physics. Boca Raton, FL: CRC Press; 2019.
Parodi K, Polf JC. In vivo range verification in particle therapy. Med Phys 2018;45:e1036–e1050.
Parodi K, Paganetti H, Shih HA, Michaud S, Loeffler JS, DeLaney TF, Liebsch NJ, Munzenrider JE, Fischman AJ, Knopf A, Bortfeld T. Patient study of in vivo verification of beam delivery and range, using positron emission tomography and computed tomography imaging after proton therapy. Int J Radiat Oncol Biol Phys 2007;68:920–934.
Patch SK, Nguyen C, Dominguez-Ramirez D, Labarbe R, Janssens G, Cammarano D, Lister J, Finch C, Lambert J, Pandey J, Bennett C, Porteous E, Chirvase C, Cohilis M, Souris K, Ono S, Lynch T. Thermoacoustic range verification during pencil beam delivery of a clinical plan to an abdominal imaging phantom. Radiother Oncol 2021;159:224–230.
Polf JC, Parodi K. Imaging particle beams for cancer treatment. Phys Today 2015;68:28–33.
Putz AMV, Burghelea TI. The solid-fluid transition in a yield stress shear thinning physical gel. Rheol Acta 2009;48:673–689.
Raldow A, Lamb J, Hong T. Proton beam therapy for tumors of the upper abdomen. Br J Radiol 2020;93 20190226.
Ramalli A, Dallai A, Guidi F, Bassi L, Boni E, Tong L, Fradella G, D'hooge J, Tortoli P. Real-time high frame rate cardiac B-mode and tissue Doppler imaging based on multiline transmission and multiline acquisition. IEEE Trans Ultrason Ferroelectr Freq Control 2018;65:2030–2041.
Ramalli A, Harput S, Bezy S, Boni E, Eckersley RJ, Tortoli P, D'Hooge J. High-frame-rate tri-plane echocardiography with spiral arrays: From simulation to real-time implementation. IEEE Trans Ultrason Ferroelectr Freq Control 2020;67:57–69.
Shakya G, Hoff SE, Wang S, Heinz H, Ding X, Borden MA. Vaporizable endoskeletal droplets via tunable interfacial melting transitions. Sci Adv 2020;6:eaaz7188.
Sheeran PS, Wong VP, McFarland RJ, Ross WD, Feingold SG, Matsunaga TO, Dayton PA. Efficacy of perfluorobutane as a phase-change contrast agent for low-energyultrasonic imaging. Proc IEEE Int Ultrason Symp 2010;904–907.
Sheeran PS, Luois SH, Mullin LB, Matsunaga TO, Dayton PA. Design of ultrasonically-activatable nanoparticles using low boiling point perfluorocarbons. Biomaterials 2012;33:3262–3269.
Shimizu J, Endoh R, Fukuda T, Inagaki T, Hano H, Asami R, Kawabata KI, Yokoyama M, Furuhata H. Safety evaluation of superheated perfluorocarbon nanodroplets for novel phase change type neurological therapeutic agents. Perspect Med 2012;1–12:25–29.
Soetanto K, Chan M. Fundamental studies on contrast images from different-sized microbubbles: analytical and experimental studies. Ultrasound Med Biol 2000;26:81–91.
Toumia Y, Cerroni B, Domenici F, Lange H, Bianchi L, Cociorb M, Brasili F, Chiessi E, D'Agostino E, Van Den Abeele K, Heymans SV, D'Hooge J, Paradossi G. Phase change ultrasound contrast agents with a photopolymerized diacetylene shell. Langmuir 2019;35:10116–10127.
Viessmann OM, Eckersley RJ, Christensen-Jeffries K, Tang MX, Dunsby C. Acoustic super-resolution with ultrasound and microbubbles. Phys Med Biol 2013;58:6447–6458.
Xie Y, Bentefour EH, Janssens G, Smeets J, Vander Stappen F, Hotoiu L, Yin L, Dolney D, Avery S, O'Grady F, Prieels D, McDonough J, Solberg TD, Lustig RA, Lin A, Teo BKK. Prompt gamma imaging for in vivo range verification of pencil beam scanning proton therapy. Int J Radiat Oncol Biol Phys 2017;99:210–218.
Zhang R, Newhauser WD. Calculation of water equivalent thickness of materials of arbitrary density, elemental composition and thickness in proton beam irradiation. Phys Med Biol 2009;54:1383–1395.
Zhang G, Harput S, Lin S, Christensen-Jeffries K, Leow CH, Brown J, Dunsby C, Eckersley RJ, Tang MX. Acoustic wave sparsely activated localization microscopy (AWSALM): Super-resolution ultrasound imaging using acoustic activation and deactivation of nanodroplets. Appl Phys Lett 2018;113 014101.
Zhu X, España S, Daartz J, Liebsch N, Ouyang J, Paganetti H, Bortfeld TR, El Fakhiri G. Monitoring proton radiation therapy with in-room PET imaging. Phys Med Biol 2011;56:4041–4057.